

# Coherent phonons in a $\text{Bi}_2\text{Se}_3$ film generated by an intense single-cycle THz pulse

A. A. Melnikov<sup>1,\*</sup>, K. N. Boldyrev<sup>1</sup>, Yu. G. Selivanov<sup>2</sup>, V. P. Martovitskii<sup>2</sup>, S. V. Chekalin<sup>1</sup>, and E. A. Ryabov<sup>1</sup>.

<sup>1</sup>*Institute for Spectroscopy RAS, Fizicheskaya 5, Troitsk, Moscow, 108840 Russia*

<sup>2</sup>*P. N. Lebedev Physics Institute RAS, Moscow, 119991 Russia*

\*e-mail: melnikov@isan.troitsk.ru

We report an observation of coherent phonons of  $E_g^1$ ,  $E_u^1$ ,  $E_g^2$ , and  $A_{1g}^2$  symmetry generated in a single-crystal film of  $\text{Bi}_2\text{Se}_3$  by an intense single-cycle THz pulse. The atomic vibrations reveal themselves through periodic anisotropic modulation of the refractive index of the film. The largest signal is detected at the frequency of 4.05 THz that corresponds to the  $E_g^2$  mode. The generation of  $E_g^2$  phonons is interpreted as resonant excitation of the Raman mode by the second harmonic of THz-driven nonlinear  $E_u^1$  oscillator, the fundamental frequency of which (2.05 THz) is approximately half that of  $E_g^2$ . The origin of nonlinearity in this case is cubic lattice anharmonicity, while generation of  $E_g^1$  (1.1 THz) and  $A_{1g}^2$  (5.3 THz) phonons is a manifestation of quartic anharmonicity that provides the frequency combination  $2\Omega(E_u^1) \approx \Omega(A_{1g}^2) - \Omega(E_g^1)$ .

## Introduction.

The development of laser sources of ultrashort pulses in mid-infrared and terahertz domains has made it possible to study highly nonequilibrium states of matter previously inaccessible in experiments with pulses at visible wavelengths. Mid-IR and THz pulses can selectively excite low-energy degrees of freedom reducing concomitant population of higher lying electronic states and avoiding generation of a hot thermalized electronic distribution. The exposure of a sample to intense low-frequency pulses tuned into resonance with a specific mode results in generation of a high-amplitude coherent wave packet on the timescales shorter than characteristic inverse rates of most relaxation processes. Such excited states are therefore convenient to use as models for studies of nonlinear effects, phase transitions, and interactions between rotational, vibrational, spin and electronic degrees of freedom in their “pure” form. The number of applications of such

an approach is growing fast [1, 2]. Among them are the control of electron-phonon interactions by intense mid-IR pulses [3-5] and photoinduced superconductivity [6, 7], THz driving of magnon resonances [8-10], control of magnetic [11, 12], electronic [13, 14] and structural [15-17] properties via coherent pumping of phonon resonances.

In the present work we study the ultrafast response of crystalline  $\text{Bi}_2\text{Se}_3$  to intense THz pulses. This solid belongs to a class of bismuth and antimony chalcogenides, which are objects of intense scientific research in two large areas. First, these crystals demonstrate unique electronic properties predicted for 3D topological insulators [18]. They are narrow bandgap insulators in the bulk, while the surface hosts Dirac-like electronic states with linear dispersion. These electrons are topologically protected from scattering and demonstrate spin-momentum locking. Second, a number of crystals from this family (e.g.  $\text{Bi}_2\text{Te}_3$  and  $\text{Sb}_2\text{Te}_3$ ) demonstrate a large thermoelectric effect, which is in part due to the considerable lattice anharmonicity. Here we focus on the structural response of  $\text{Bi}_2\text{Se}_3$ .

The decay traces measured in our experiment contain oscillations at four frequencies of 1.1, 2.05, 4.05, and 5.30 THz (with a maximal error of  $\sim 0.05$  THz), which correspond to the optical phonon modes of  $E_g^1$ ,  $E_u^1$ ,  $E_g^2$ , and  $A_{1g}^2$  symmetry. These oscillations are caused by coherent motion of atoms of  $\text{Bi}_2\text{Se}_3$  induced by a single pump THz pulse and are commonly referred to as coherent phonons [19-28].

Generation of coherent phonons by a THz pulse is a rather interesting observation. Indeed, the duration of THz pulses in our case is about 1 ps that is almost equal to (for  $E_g^1$  mode) or considerably larger than (for other modes) the periods of corresponding phonon modes. Therefore, if one considers such standard mechanisms of coherent phonon generation as ISRS [29], TSRS [30] or DECP [31], one should not expect the appearance of coherent Raman active phonons in the THz-induced transient reflectivity or transmission of  $\text{Bi}_2\text{Se}_3$ . One possible exception is coherent driving of phonons that are both IR and Raman active [32]. However, as concerns bulk phonon modes observed in our experiments, this is not the case. Moreover,  $E_g^2$  and  $A_{1g}^2$  modes are situated outside the spectrum of the THz excitation pulse, and cannot be driven by the electric field of the THz pulse directly even at the  $\text{Bi}_2\text{Se}_3/\text{BaF}_2$  interface, where bulk symmetry breaks. Therefore, in order to explain THz-induced coherent phonons in  $\text{Bi}_2\text{Se}_3$  some higher-order processes should be considered.

Recently similar experiments were reported in [33] and [34]. The appearance of oscillations at the frequency of  $E_g^2$  Raman active mode was interpreted as vibrationally induced symmetry breaking in the bulk and sum-frequency Raman scattering respectively. In contrast to those

reports we argue here that the coherent generation of Raman active modes by an intense THz pulse is a result of lattice anharmonicity and multi-phonon processes somewhat similar to the ionic Raman scattering proposed in [15].

## Experimental details.

The sample of  $\text{Bi}_2\text{Se}_3$  used in our experiments was grown on a (111)-oriented  $\text{BaF}_2$  substrate by molecular beam epitaxy (MBE) using standard effusion cells for high purity elemental Se and binary  $\text{Bi}_2\text{Se}_3$  compound [35, 36]. The single crystalline nature of the film was supported by a streaky RHEED pattern during epitaxial growth. Immediately after growth, the film on the substrate was cooled down to the room temperature and, in order to protect the film surface from exposure to the atmospheric air, a  $\text{BaF}_2$  cap layer was deposited in the same growth chamber from an additional cell with a  $\text{BaF}_2$  source. The obtained  $\text{Bi}_2\text{Se}_3$  film had a high structural quality and a thickness of  $d = 22.3$  nm determined from the (006) Bragg peak thickness fringes (Fig. 1).

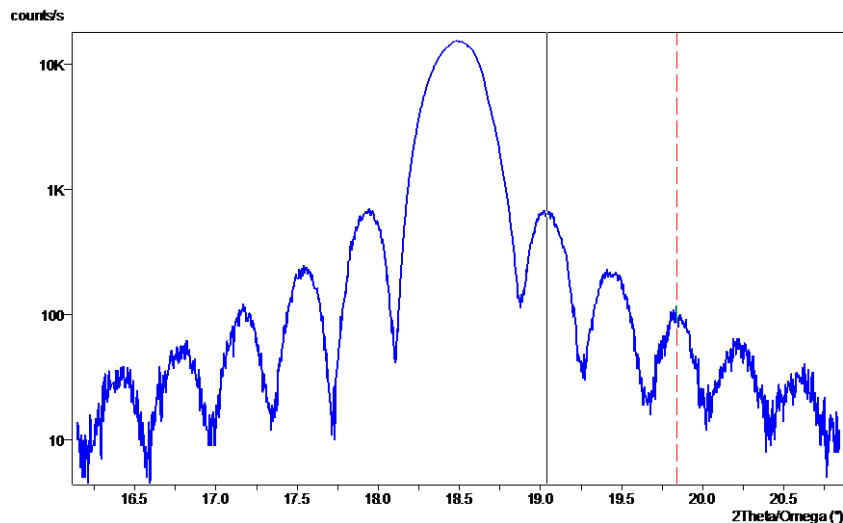


Fig. 1. XR-XRD of  $\text{Bi}_2\text{Se}_3$  (006) reflection on a logarithmic scale. Vertical solid and dashed lines indicate Bragg satellite angular positions.

Thickness of the  $\text{BaF}_2$  cap layer was extracted from x-ray reflectivity (XRR) curves (not shown here). The best fit for the measured and computed thicknesses resulted in 24 and 28 nm for the  $\text{Bi}_2\text{Se}_3$  and  $\text{BaF}_2$  layers, respectively. The morphological quality of a  $\text{Bi}_2\text{Se}_3$  film could be evaluated removing the cap  $\text{BaF}_2$  layer in 0.1% vol. HCl water solution and scanning the film in an atomic force microscope (AFM). Figure 2 shows a typical AFM image of the restored surface of an epitaxial  $\text{Bi}_2\text{Se}_3$  film with RMS roughness of 0.7 nm. The height of the terrace steps is about 1 nm. This corresponds to the thickness of the building block of  $\text{Bi}_2\text{Se}_3$  lattice structure, the so called quintuple layer, which consists of a sequence of five Se-Bi-Se-Bi-Se atomic sheets.

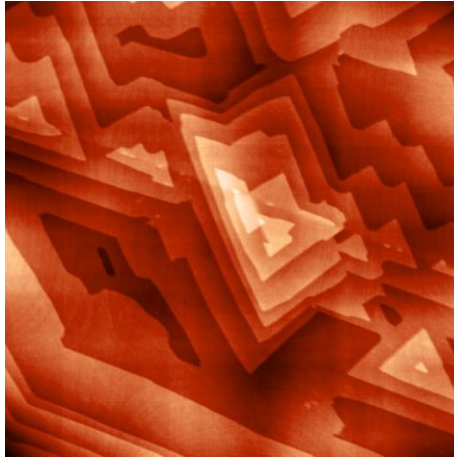


Fig. 2. AFM 5x5  $\mu\text{m}$  image of a typical  $\text{Bi}_2\text{Se}_3$  film. RMS = 0.7 nm.

Terahertz pulses with a duration of about 1 ps were generated in a lithium niobate crystal using the “optical rectification of femtosecond laser pulses with tilted fronts” technique (a description of this method can be found elsewhere [37]). THz radiation was focused into the sample using parabolic mirrors and the resulting peak electric field reached values of about 1 MV/cm. To detect THz-induced changes we used a weak 35 fs probe pulse at 800 nm. Before the sample it was linearly polarized at an angle of  $45^\circ$  relative to the polarization of pump THz pulses, which was vertical. Both pump and probe beams were almost normal to the sample plane. The ellipticity of the probe pulse polarization induced by THz electric field was characterized measuring intensities of its two orthogonal polarization components by means of a quarter wave plate, Wollaston prism and a pair of photodiodes placed after the sample. The corresponding ratio  $I_x/I_y$  recorded at a number of values of the delay time between pump and probe pulses served as final data for further analysis and interpretation.

## Results and discussion.

A typical waveform of the pump THz pulse is shown in Fig. 3. It was measured placing a ZnTe crystal in the position of the sample. In this case  $I_x/I_y$  is proportional to the THz electric field strength as soon as the effect responsible for depolarization of the probe pulse is the linear electro-optic effect (or Pockels effect). The long-lived oscillations after the pulse are caused by the absorption in air due to rotational transitions. Rotational lines seen as dips in the spectrum are in fact very narrow. This would be clear if the maximal delay time was 1-2 orders of magnitude longer than the one used in our measurements. The only effect of air in our experiments is a certain decrease of the peak THz electric field, which we neglect during the data analysis, as soon as relative amplitudes of the modes are compared.

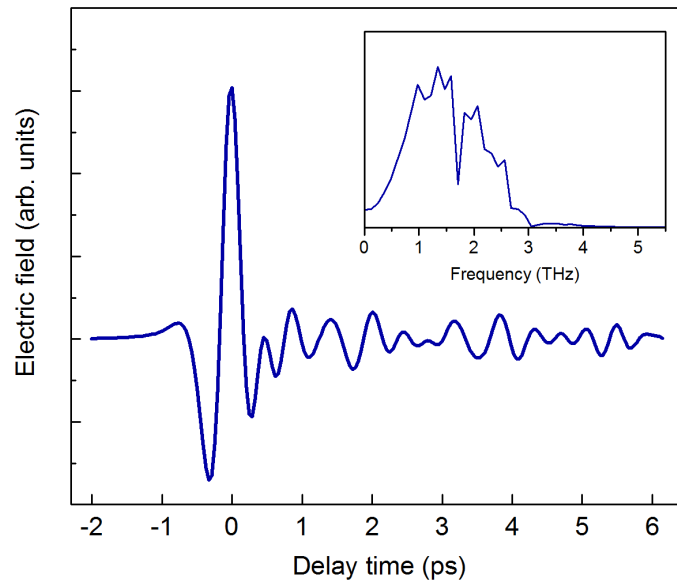


Fig. 3. Electric field and the spectrum (in the inset) of the pump THz pulse in the air-filled setup.

The result of excitation of the  $\text{Bi}_2\text{Se}_3$  film by such a THz pulse is shown in Fig. 4 for two cases: the signal with smaller amplitude was measured when the THz setup was filled with air, while the signal with larger amplitude - when the setup was filled with gaseous nitrogen. In the first case the signal is weaker, which is natural, as soon as a fraction of THz pulse energy is absorbed in air. Spectra of the decay traces are presented in the inset to Fig. 4.

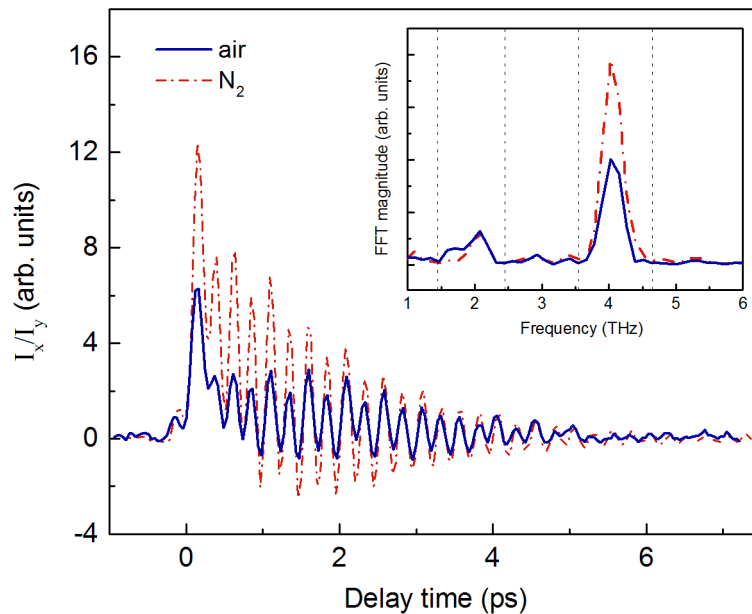


Fig. 4. THz-induced response of the  $\text{Bi}_2\text{Se}_3/\text{BaF}_2$  sample measured under ambient conditions (solid) and in the nitrogen-filled setup (dash-dot). The inset shows spectra of the transient signals. Dashed lines indicate frequency ranges of the band pass filters used to extract temporal components.

They contain two spectral lines centered at 2.05 and 4.05 THz. We assign oscillations at 2.05 THz to the  $E_u^1$  phonon mode of  $\text{Bi}_2\text{Se}_3$  resonantly excited by the THz pump pulse [38, 39]. This mode is IR active and the corresponding line can be seen near  $67 \text{ cm}^{-1}$  (2 THz) in the reflectance spectrum of the  $\text{Bi}_2\text{Se}_3/\text{BaF}_2$  sample shown in Fig. 5. The amplitude of this line is independent on the polarization of light due to the  $D_{3d}^5$  symmetry of the bulk  $\text{Bi}_2\text{Se}_3$ . The central frequency of the peak falls inside the spectrum of the pump THz pulse and therefore  $E_u^1$  mode can be coherently driven by its electric field irrespective of the sample orientation. More complex is the situation with oscillations at 4.05 THz, which we interpret as coherent phonons of  $E_g^2$  symmetry. This mode is not IR but Raman active and its frequency lies beyond the spectrum of the THz pump pulse. Thus,  $E_g^2$  vibrations cannot be excited directly by the THz electric field.

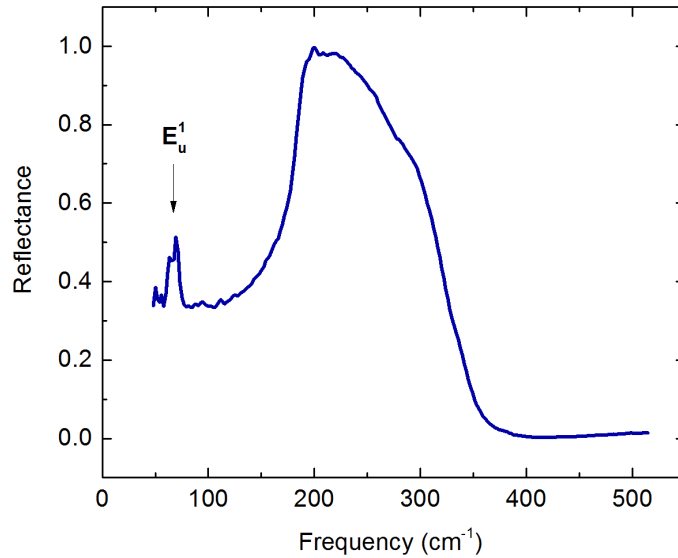


Fig. 5. Reflectance spectrum of the  $\text{Bi}_2\text{Se}_3/\text{BaF}_2$  sample. The line near  $67 \text{ cm}^{-1}$  (2 THz) is due to the  $E_u^1$  phonon mode, while the intense broad band  $150 - 350 \text{ cm}^{-1}$  is caused by phonons in the  $\text{BaF}_2$  substrate (the so-called reststrahlen band).

From our data it follows that if the amplitude of  $E_u^1$  mode increases linearly with the THz electric field (as it should be for a linear absorption process), then the amplitude of  $E_g^2$  oscillations demonstrates quadratic growth. To show that we have compared the amplitudes of these frequency components measured at two different values of THz electric field strength (in air and in  $\text{N}_2$ ). For that purpose we extract temporal contribution of each spectral component applying FFT band pass filters 1.45 - 2.45 THz and 3.55 - 4.65 THz. The result is shown in Fig. 6. We have found that the ratio of amplitudes of 2.05 THz oscillations measured in  $\text{N}_2$  and in air is 1.66, while for the 4.05 THz mode it is 2.53, which is close to  $1.66^2 \approx 2.76$ . This result agrees

with previous measurements [33, 34], where it was found that  $E_u^1$  coherent amplitude grows linearly with the THz electric field strength, while the  $E_g^2$  one - quadratically. Therefore, some nonlinear second-order process should be responsible for the generation of coherent  $E_g^2$  phonons.

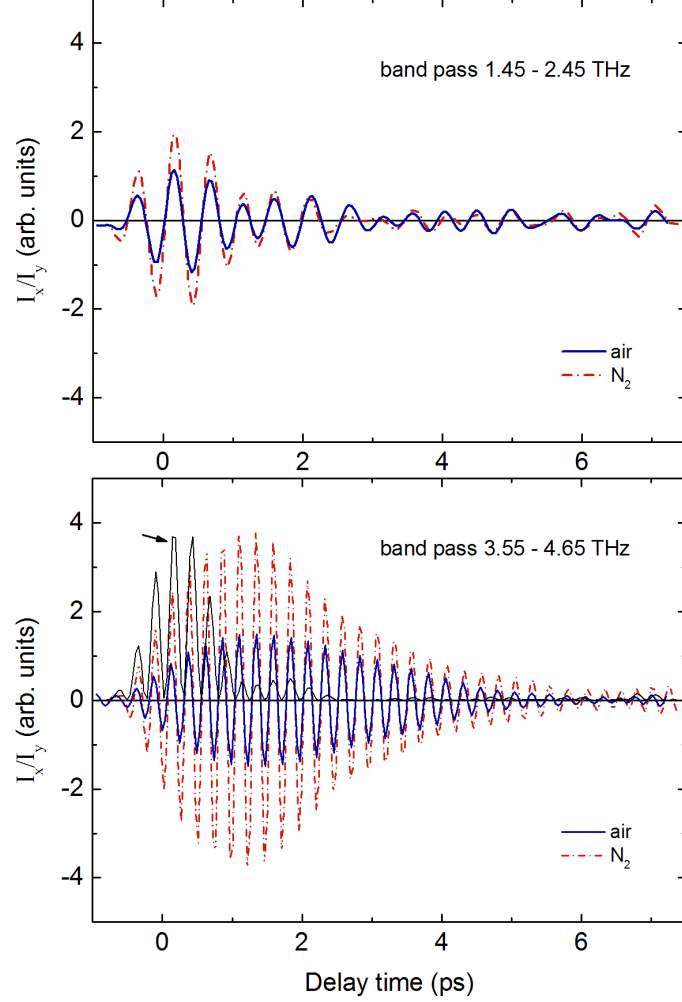


Fig. 6. Temporal components of decay traces from Fig. 4 corresponding to frequency bands near 2 THz and 4 THz obtained using FFT band pass filters. The lower panel shows also the 2 THz temporal component squared (thin black line, indicated by an arrow).

A straightforward way to interpret the observations is to suppose that this process is a three-phonon interaction due to lattice anharmonicity. Indeed,  $\text{Bi}_2\text{Te}_3$  belongs to a group of solids that are described by a common formula  $\text{Bi}_2\text{Te}_{3-x}\text{Se}_x$  and are known as good thermoelectrics [40]. The figure of merit that is used to evaluate their efficiency is inversely proportional to the thermal conductivity [41]. The latter, in turn, is small when the scattering of longitudinal acoustic phonons is strong. In  $\text{Bi}_2\text{Te}_{3-x}\text{Se}_x$  materials and several other thermoelectrics (like  $\text{Pb}_{1-x}\text{Sn}_x\text{Te}$  [42] and  $\text{SnSe}$  [41, 43]) the efficient scattering channel is provided by TO phonon modes that are considerably softened due to lattice anharmonicity [40]. In our case the  $E_u^1$  mode

that is highly excited by the intense THz pulse is in fact a TO mode, and it is natural to expect nonlinear effects due to inelastic phonon-phonon interactions. In particular, annihilation of two  $E_u^1$  phonons can generate one  $E_g^2$  phonon - this process is allowed by symmetry [15] and conserves energy, as soon as the frequency of the  $E_g^2$  mode is approximately twice the frequency of the  $E_u^1$  mode. We note here that recently lattice anharmonicity was invoked to explain THz excitation of Raman active modes in CdWO<sub>4</sub> [44].

In case of Bi<sub>2</sub>Se<sub>3</sub> the excitation of coherent Raman phonons can be modelled using the approach proposed in [15]. The equation of motion for the Raman phonon mode can be written as

$$\ddot{Q}_R + \Omega_R^2 Q_R = A Q_I^2 \quad (1)$$

where  $R$  and  $I$  denote Raman and IR active modes, and  $A$  is the anharmonicity constant. The driving term  $A Q_I^2$  originates from the interaction term  $A Q_I^2 Q_R$  that describes the three-phonon interaction. In the latter two IR active phonons interact with one Raman active phonon. The IR active mode is driven by the electric field of the pulse

$$E(t) = E_0 \sin(\Omega_I t) F(t) \quad (2)$$

where  $F(t)$  is the pulse envelope. This is probably not the best way to describe the real nearly single-cycle THz pulse but nevertheless we use Eq. 2 here as a convenient demonstrative model. The equation of motion for the driven IR active mode is

$$\ddot{Q}_I + \Omega_I^2 Q_I = B E_0 \sin(\Omega_I t) F(t) \quad (3)$$

where constant  $B$  depends on the properties of the phonon mode, and damping is neglected for simplicity (as in Eq. 1). Therefore, after the action of the pulse  $Q_I(t) \propto \cos(\Omega_I t)$ , and the driving term in (1) will contain two contributions: the first one is constant, while the second one  $\propto \cos(2\Omega_I t)$ . The quasiconstant (in fact, it represents a convolution of a step function and  $F(t)$ ) driving force is considered in [15] as a source of transient lattice displacement by analogy with nonlinear optical rectification. This force, however, can excite  $Q_R$  only if  $\Omega_I \gg \Omega_R$ , which is not the case for Bi<sub>2</sub>Se<sub>3</sub>, as its optical phonon modes lie in the THz range and have frequencies of the same order. Nevertheless, coherent Raman phonons can be resonantly excited by the second term  $\propto \cos(2\Omega_I t)$  if  $\Omega_R = 2\Omega_I$ , and in Bi<sub>2</sub>Se<sub>3</sub> this condition is fulfilled, as soon as  $\Omega(E_g^2) \approx 2\Omega(E_u^1)$ .

In order to find an exact temporal dependence of the driving force one should take into account the real form of the THz pulse and the damping of the  $E_u^1$  mode. However, it is possible to obtain a realistic model of the force simply by squaring the corresponding temporal

component of the signal extracted using the 1.45 - 2.45 THz FFT filter. The result is shown in Fig. 6 by a black line. We see that due to rather high damping of the  $E_u^1$  mode the force has a duration of  $\sim 1$  ps - approximately twice longer than the duration of a hypothetical nonlinear force proportional to the squared electric field of the THz pulse. Such relatively long action of a driving force should lead to a considerable delay of the oscillating signal at 4.05 THz. Indeed, we can see already in raw data in Fig. 4 that the amplitude of  $E_g^2$  vibrations increases gradually and reaches maximum only after  $\sim 1-1.5$  ps. For the filtered trace in the lower panel of Fig. 6 the effect is even more pronounced - the maximal amplitude of oscillations is reached when the driving force decays almost completely. This observation speaks in favor of our assumption that highly excited anharmonic  $E_u^1$  lattice vibrations provide the force that generates coherent Raman active phonons.

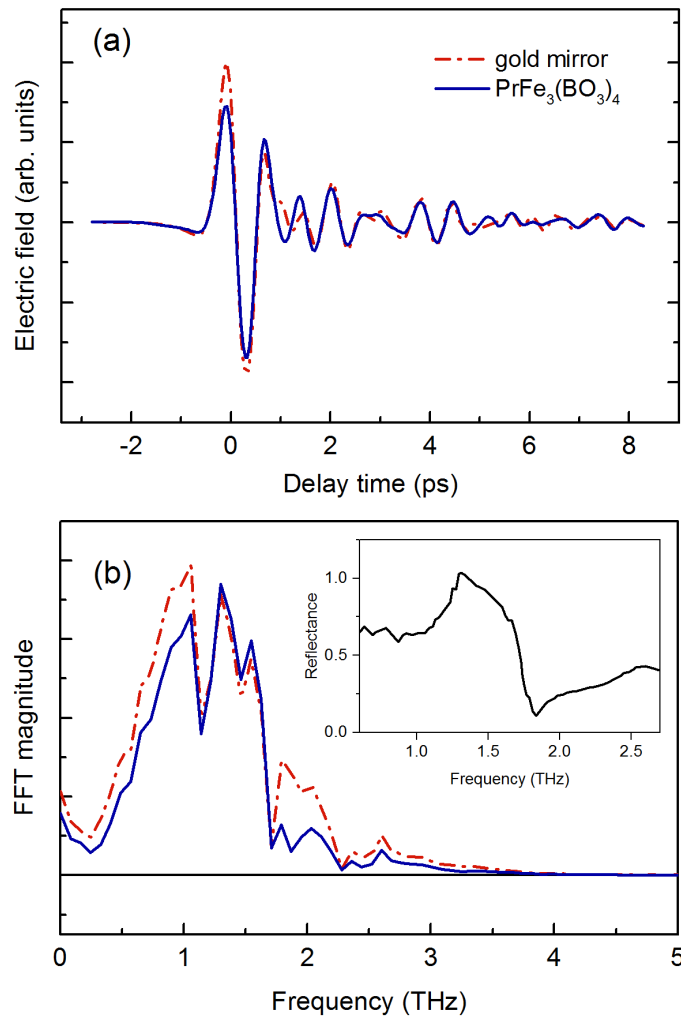


Fig. 7. (a) Electric field of the pump THz pulse reflected from a gold mirror (dash-dot) and from the PrFe<sub>3</sub>(BO<sub>3</sub>)<sub>4</sub> crystal (solid). (b) Spectra of the THz waveforms shown in (a). The inset to panel (b) shows the reflectance spectrum of PrFe<sub>3</sub>(BO<sub>3</sub>)<sub>4</sub>.

In order to check the resonant character of the oscillatory THz response of  $\text{Bi}_2\text{Se}_3$  we have performed an additional experiment, in which we filtered the pump THz radiation to selectively attenuate the spectral band near 2 THz. For that purpose we used a crystal of  $\text{PrFe}_3(\text{BO}_3)_4$  that was at hand, however, it is possible to use any other suitable filter. The reflectance spectrum of  $\text{PrFe}_3(\text{BO}_3)_4$  is shown in the inset to Fig. 7(b) [45]. At  $\sim 1.7$  THz the reflectance experiences a sharp drop and remains low near 2 THz. If we substitute one of the gold mirrors in the pump channel by this crystal, the amplitude of the THz pulse will be reduced by a factor of 1.24, while the spectral amplitude near 2 THz - by  $\sim 2$ .

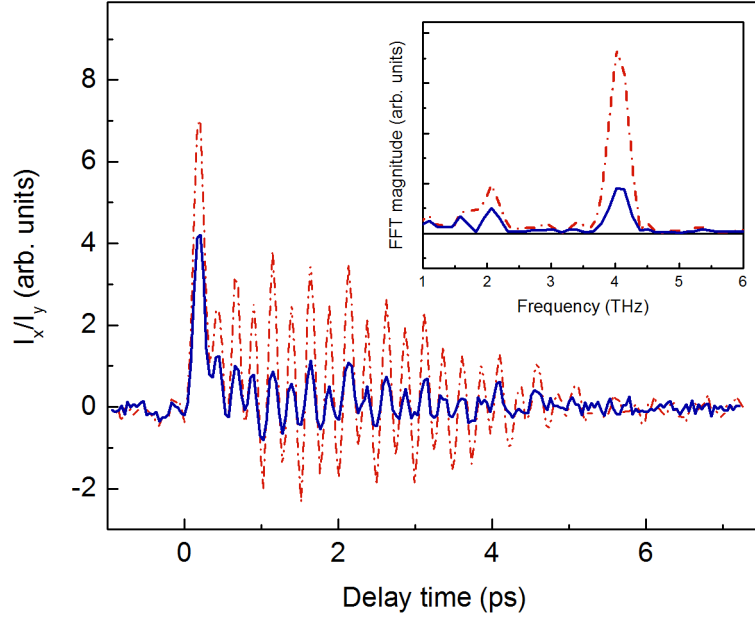


Fig. 8. THz response of  $\text{Bi}_2\text{Se}_3$  measured using THz pulses reflected from a gold mirror (dash-dot) and from the  $\text{PrFe}_3(\text{BO}_3)_4$  crystal (solid). The inset shows spectra of these signals.

At the same time, as follows from Fig. 8, the amplitude of  $E_g^2$  coherent phonons will decrease by a factor of  $\sim 4$  and not 1.5 as it would be if the response near 4 THz was proportional to the squared electric field strength. This result shows that the second-order lattice response of  $\text{Bi}_2\text{Se}_3$  is determined by the spectral amplitude of pump THz radiation near 2 THz, or, in other words, requires a resonance with the  $E_u^1$  phonon mode.

Next, we discuss the dependence of the coherent phonon amplitudes on the sample orientation angle  $\alpha$ . Figure 9 shows decay traces measured at  $\alpha = 0^\circ$  and  $\alpha = 90^\circ$  keeping the angle between polarization vectors of the pump and probe pulses fixed ( $45^\circ$ ). The angle  $\alpha = 0^\circ$  corresponds to the maximal coherent amplitude of the  $E_u^1$  mode, while at  $\alpha = 90^\circ$  oscillations at 2.05 THz disappear (or their amplitude decreases below the noise level). The amplitude of the  $E_g^2$  mode, in contrast, remains almost unchanged. This behavior is illustrated more clearly by

Fig. 10, which contains spectra of decay traces measured at three values of  $\alpha$  ( $0^\circ$ ,  $45^\circ$ , and  $90^\circ$ ). The invariance of  $E_g^2$  amplitude is the consequence of  $D_{3d}^5$  symmetry of the bulk  $\text{Bi}_2\text{Se}_3$  as soon as for such crystals the intensities of Raman lines do not depend on the orientation of crystallographic axes in the geometry used in our measurements [46].

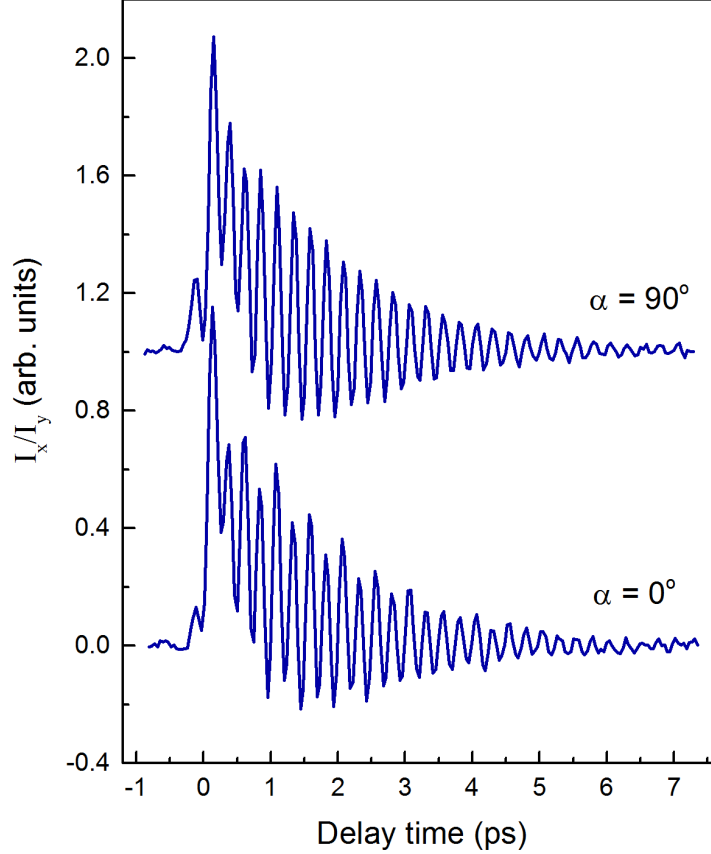


Fig. 9. Photoinduced response of  $\text{Bi}_2\text{Se}_3$  measured at two orientations of the sample.

The situation is different for the  $E_u^1$  phonon mode. This mode is IR active and damped oscillations of polarization that follow its coherent excitation by the THz pulse could in principle reveal themselves through the linear electro-optic effect (or Pockels effect) and be detected in our experimental layout. However, Pockels effect in bulk  $\text{Bi}_2\text{Se}_3$  is forbidden by symmetry due to the presence of the center of inversion. It is nevertheless allowed at the surface of the crystal, which has  $C_{3v}$  symmetry. It can be shown that in this case the magnitude of the electro-optic effect follows the same dependence on the sample orientation as we have observed (i.e. vanishes at  $\alpha = 90^\circ$ ). However, the derivation is rather cumbersome and we refer here to the case of lithium niobate, which has  $C_{3v}$  symmetry in the bulk and demonstrates the same behavior upon crystal rotation in stationary electro-optic measurements (see e.g. [47]). Thus, relying on these results, we can conclude that though  $E_u^1$  mode is excited across the whole volume of the  $\text{Bi}_2\text{Se}_3$  film, the corresponding signal at 2.05 THz originates from the  $\text{Bi}_2\text{Se}_3/\text{BaF}_2$  interfaces.

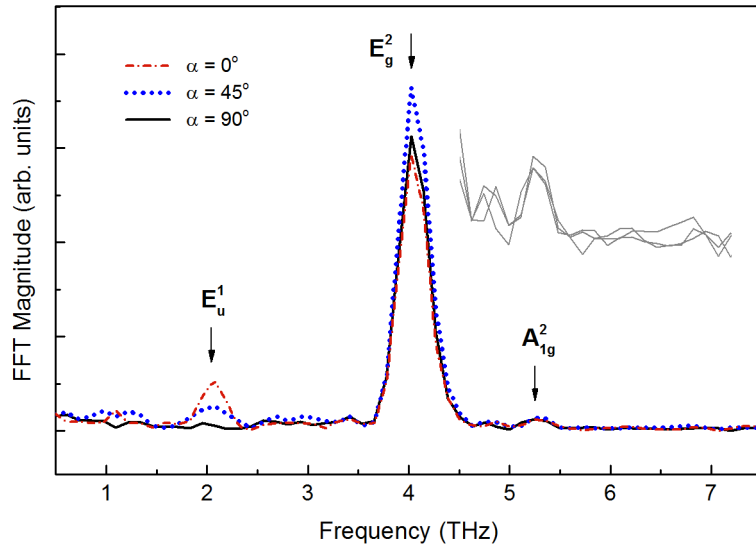


Fig. 10. Spectra of decay traces measured at three values of the sample orientation angle  $\alpha$ . The magnified region containing  $A_{1g}^2$  mode is also shown.

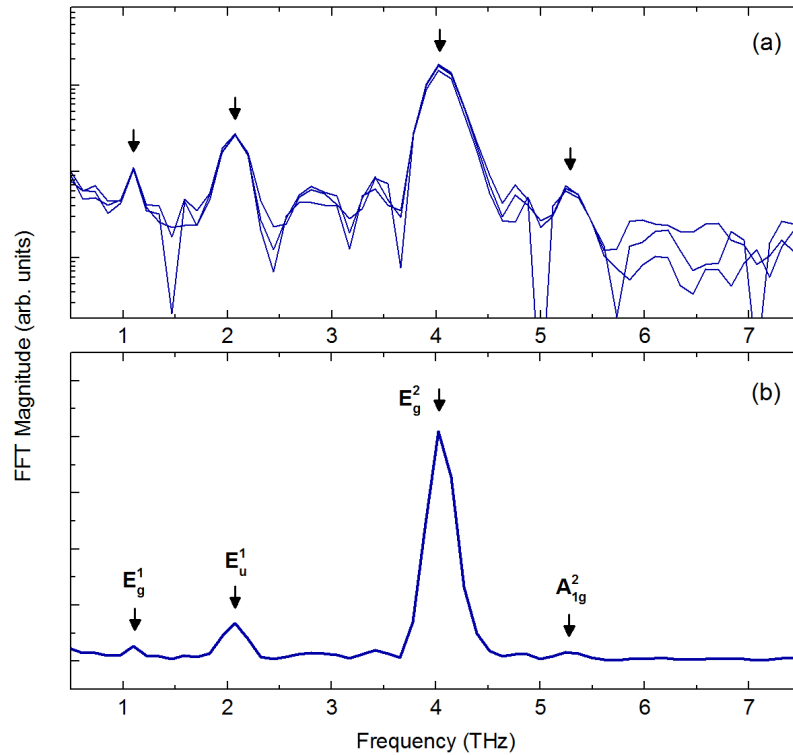


Fig. 11. (a) - Spectra of three decay traces measured at optimal conditions (logarithmic scale along y-axis). (b) - Averaged spectrum.

Figure 10 illustrates one more interesting result, i.e. the presence of the  $A_{1g}^2$  peak in the spectra. These coherent phonons are fully symmetric and should not be detected in an ideal anisotropic detection system. Their appearance probably indicates incomplete cancellation of the isotropic signal in process of measurement of  $I_x/I_y$ . Spectra in Fig. 11 that were detected under optimal conditions (filling the setup with  $N_2$  and accumulating data from a larger amount of pulses) contain also one more peak at the frequency of  $\sim 1.1$  THz. It has very small amplitude,

but nevertheless is reproduced in consecutive measurements. This frequency corresponds to the  $E_g^1$  Raman active mode of  $\text{Bi}_2\text{Se}_3$  [48]. The generation of  $A_{1g}^2$  and  $E_g^1$  coherent phonons cannot be interpreted taking into account only three-phonon processes by analogy with the generation of  $E_g^2$  mode, because energy is not conserved in this case. However, it is reasonable to consider also four-phonon processes (recently it was proposed that quartic anharmonicity causes anomalous hardening of  $A_g^1$  mode in  $\text{Bi}_2\text{Te}_3$  [40]). In  $\text{Bi}_2\text{Se}_3$  such a process implies interaction of two  $E_u^1$ , one  $E_g^1$  and one  $A_{1g}^2$  phonons that have a suitable combination of frequencies  $2\Omega(E_u^1) \approx \Omega(A_{1g}^2) - \Omega(E_g^1)$ .

## Conclusion.

In summary, we have measured the response of a single crystal  $\text{Bi}_2\text{Se}_3$  film to a single-cycle THz pulse. We have found that the intense resonant excitation of IR active  $E_u^1$  mode leads to the generation of  $E_g^1$ ,  $E_g^2$ , and  $A_{1g}^2$  coherent Raman active phonons. We conclude that this effect is caused by three- and four-phonon interactions in the anharmonic crystal lattice of  $\text{Bi}_2\text{Se}_3$ . The origin of the force that drives Raman modes is the nonlinear motion of  $E_u^1$  oscillator. Thus, the observed effect differs from conventional Raman scattering, for which the driving term acts only through electronic degrees of freedom. The force is not impulsive like in ISRS, and not displacive like in DECP, but periodic and has a certain duration defined by the THz pulse duration and the damping rate of the driven  $E_u^1$  mode.

Coherent  $E_g^2$  phonons should also be generated via this process in related crystals of  $\text{Bi}_2\text{Te}_3$  and  $\text{Sb}_2\text{Te}_3$ , for which  $\Omega(E_g^2) \approx 2\Omega(E_u^1)$  as in  $\text{Bi}_2\text{Se}_3$ . It would be interesting also to detect other THz-induced coherent Raman phonons in the whole family of compounds. Using such control parameters as doping and temperature, it could be possible to investigate the interplay of cubic and quartic lattice anharmonicities in these solids. The approach used here can also be applied in studies of lattice anharmonicities in a broader class of thermoelectrics, many of which have soft TO modes.

## Acknowledgements.

This work was supported by the Ministry of Education and Science of the Russian Federation (project # RFMEFI61316X0054).

## References.

1. T. Kampfrath, K. Tanaka, and K. A. Nelson. Resonant and nonresonant control over matter and light by intense terahertz transients, *Nat. Photonics* **7**, 680-690 (2013).
2. D. Nicoletti, A. Cavalleri. Nonlinear light-matter interaction at terahertz frequencies. *Adv. Opt. Photon.* **8** 401-464 (2016).
3. I. Gierz, M. Mitrano, H. Bromberger, C. Cacho, R. Chapman, E. Springate, S. Link, U. Starke, B. Sachs, M. Eckstein, T. O. Wehling, M. I. Katsnelson, A. Lichtenstein, and A. Cavalleri. Phonon-pump extreme-ultraviolet-photoemission probe in graphene: anomalous heating of Dirac carriers by lattice deformation. *Phys. Rev. Lett.* **114**, 125503 (2015).
4. E. Pomarico, M. Mitrano, H. Bromberger, M. A. Sentef, A. Al-Temimy, C. Coletti, A. Stöhr, S. Link, U. Starke, C. Cacho, R. Chapman, E. Springate, A. Cavalleri, and I. Gierz. Enhanced electron-phonon coupling in graphene with periodically distorted lattice. *Phys. Rev. B* **95**, 024304 (2017).
5. M. A. Sentef. Light-enhanced electron-phonon coupling from nonlinear electron-phonon coupling. *Phys. Rev. B* **95**, 205111 (2017).
6. M. Mitrano, A. Cantaluppi, D. Nicoletti, S. Kaiser, A. Perucchi, S. Lupi, P. Di Pietro, D. Pontiroli, M. Riccò, S. R. Clark, D. Jaksch, and A. Cavalleri. Possible light-induced superconductivity in  $K_3C_{60}$  at high temperature. *Nature* **530**, 461–464 (2016).
7. D. M. Kennes, E. Y. Wilner, D. R. Reichman, and A. J. Millis, Transient superconductivity from electronic squeezing of optically pumped phonons. *Nat. Phys.* **13**, 479–483 (2017).
8. T. Kubacka, J. A. Johnson, M. C. Hoffmann, C. Vicario, S. de Jong, P. Beaud, S. Grübel, S.-W. Huang, L. Huber, L. Patthey, Y.-D. Chuang, J. J. Turner, G. L. Dakovski, W.-S. Lee, M. P. Minitti, W. Schlotter, R. G. Moore, C. P. Hauri, S. M. Koohpayeh, V. Scagnoli, G. Ingold, S. L. Johnson, U. Staub. Large-amplitude spin dynamics driven by a THz pulse in resonance with an electromagnon. *Science* **343**, 1333 (2014).
9. P. Bownan, S. A. Trugman, J. Bownan, J.-X. Zhu, N. J. Hur, A. J. Taylor, D. A. Yarotski, and R. P. Prasankumar. Probing ultrafast spin dynamics through a magnon resonance in the antiferromagnetic multiferroic  $HoMnO_3$ . *Phys. Rev. B* **94**, 100404 (R) (2016).
10. S. Baierl, J. H. Mentink, M. Hohenleutner, L. Braun, T.-M. Do, C. Lange, A. Sell, M. Fiebig, G. Woltersdorf, T. Kampfrath, and R. Huber. Terahertz-driven nonlinear spin response of antiferromagnetic nickel oxide. *Phys. Rev. Lett.* **117**, 197201 (2016).

11. T. F. Nova, A. Cartella, A. Cantaluppi, M. Foerst, D. Bossini, R. V. Mikhaylovskiy, A. V. Kimel, R. Merlin, A. Cavalleri. An effective magnetic field from optically driven phonons. *Nat. Phys.* **13**, 132–136 (2017).
12. D. M. Juraschek, M. Fechner, A. V. Balatsky, N. A. Spaldin. Dynamical multiferroicity. *Phys. Rev. Mat.* **1**, 014401 (2017).
13. M. Rini, Ra. Tobey, N. Dean, J. Itatani, Y. Tomioka, Y. Tokura, R. W. Schoenlein, and A. Cavalleri. Control of the electronic phase of a manganite by mode-selective vibrational excitation. *Nature* **449**, 72-74 (2007).
14. V. Esposito, M. Fechner, R. Mankowsky, H. Lemke, M. Chollet, J.M. Glowia, M. Nakamura, M. Kawasaki, Y. Tokura, U. Staub, P. Beaud, and M. Först. Nonlinear electron-phonon coupling in doped manganites. *Phys. Rev. Lett.* **118**, 247601 (2017).
15. M. Först, C. Manzoni, S. Kaiser, Y. Tomioka, Y. Tokura, R. Merlin and A. Cavalleri. Nonlinear phononics as an ultrafast route to lattice control. *Nat. Phys.* **7**, 854–856 (2011).
16. D.M. Juraschek, M. Fechner, and N.A. Spaldin. Ultrafast structure switching through nonlinear phononics. *Phys. Rev. Lett.* **118**, 054101 (2017).
17. R. Mankowsky, M. Först, T. Loew, J. Porras, B. Keimer, and A. Cavalleri. Coherent modulation of the  $\text{YBa}_2\text{Cu}_3\text{O}_{6+x}$  atomic structure by displacive stimulated ionic Raman scattering. *Phys. Rev. B* **91**, 094308 (2015).
18. M. Z. Hasan and C. L. Kane. Colloquium: Topological insulators. *Rev. Mod. Phys.* **82**, 3045 (2010).
19. T. Dekorsy, G. C. Cho, and H. Kurz. Coherent phonons in condensed media. *Light Scattering in Solids VIII*, editors: M. Cardona and G. Güntherodt (Springer, Berlin, 2000), Ch. 4.
20. N. Kamaraju, S. Kumar and A. K. Sood. Temperature-dependent chirped coherent phonon dynamics in  $\text{Bi}_2\text{Te}_3$  using high-intensity femtosecond laser pulses. *EPL* **92**, 47007 (2010).
21. J. Qi, X. Chen, W. Yu, P. Cadden-Zimansky, D. Smirnov, N. H. Tolk, I. Miotkowski, H. Cao, Y. P. Chen, Y. Wu, S. Qiao, and Z. Jiang. Ultrafast carrier and phonon dynamics in  $\text{Bi}_2\text{Se}_3$  crystals. *Appl. Phys. Lett.* **97**, 182102 (2010).
22. K. Norimatsu, J. Hu, A. Goto, K. Igarashi, T. Sasagawa, K. G. Nakamura. Coherent optical phonons in a  $\text{Bi}_2\text{Se}_3$  single crystal measured via transient anisotropic reflectivity. *Solid State Commun.* **157**, 58–61 (2013).

23. K. Norimatsu, M. Hada, S. Yamamoto, T. Sasagawa, M. Kitajima, Y. Kayanuma, and K. G. Nakamura. Dynamics of all the Raman-active coherent phonons in  $\text{Sb}_2\text{Te}_3$  revealed via transient reflectivity. *J. Appl. Phys.* **117**, 143102 (2015).
24. M. Weis, K. Balin, R. Rapacz, A. Nowak, M. Lejman, J. Szade, and P. Ruello. Ultrafast light-induced coherent optical and acoustic phonons in few quintuple layers of the topological insulator  $\text{Bi}_2\text{Te}_3$ . *Phys. Rev. B* **92**, 014301 (2015).
25. O. V. Misochko, A. A. Melnikov, S. V. Chekalin, and A. Yu. Bykov. Features of coherent phonons of the strong topological insulator  $\text{Bi}_2\text{Te}_3$ . *JETP Lett.* **102**, 235–241 (2015).
26. O. V. Misochko, J. Flock, and T. Dekorsy. Polarization dependence of coherent phonon generation and detection in the three-dimensional topological insulator  $\text{Bi}_2\text{Te}_3$ . *Phys. Rev. B* **91**, 174303 (2015)
27. A. Y. Bykov, T. V. Murzina, N. Olivier, G. A. Wurtz, and A. V. Zayats. Coherent lattice dynamics in topological insulator  $\text{Bi}_2\text{Te}_3$  probed with time-resolved optical second-harmonic generation. *Phys. Rev. B* **92**, 064305 (2015).
28. E. Golias and J. Sanchez-Barriga. Observation of antiphase coherent phonons in the warped Dirac cone of  $\text{Bi}_2\text{Te}_3$ . *Phys. Rev. B* **94**, 161113 (R) (2016).
29. L. Dhar, J. A. Rogers, K. A. Nelson. Time-resolved vibrational spectroscopy in the impulsive limit. *Chem. Rev.* **94**, 157 (1994).
30. D. M. Riffe and A. J. Sabbah. Coherent excitation of the optic phonon in Si: Transiently stimulated Raman scattering with a finite-lifetime electronic excitation. *Phys. Rev. B* **76**, 085207 (2007).
31. H. J. Zeiger, J. Vidal, T. K. Cheng, E. P. Ippen, G. Dresselhaus, and M. S. Dresselhaus. Theory for displacive excitation of coherent phonons. *Phys. Rev. B* **45**, 768 (1992).
32. T. Huber, M. Ranke, A. Ferrer, L. Huber, and S. L. Johnson. Coherent phonon spectroscopy of non-fully symmetric modes using resonant terahertz excitation. *Appl. Phys. Lett.* **107**, 091107 (2015).
33. P. Bowlan, J. Bowlan, S. A. Trugman, R. Valdés Aguilar, J. Qi, X. Liu, J. Furdyna, M. Dobrowolska, A. J. Taylor, D. A. Yarotski, and R. P. Prasankumar. Probing and controlling terahertz-driven structural dynamics with surface sensitivity. *Optica* **4**, 383-387 (2017).
34. L. Braun. Electron and phonon dynamics in topological insulators at THz frequencies. Freie Universität Berlin, Germany (2016).

35. A. Yu. Kuntsevich, A. A. Gabdullin, V. A. Prudkoglyad, Yu. G. Selivanov, E. G. Chizhevskii, and V. M. Pudalov. Low temperature Hall effect in bismuth chalcogenides thin films. *Phys. Rev. B* **94**, 235401 (2016).
36. L. N. Oveshnikov, V. A. Prudkoglyad, E. I. Nekhaeva, A. Yu. Kuntsevich, Yu. G. Selivanov, E. G. Chizhevskii, B. A. Aronzon. Magnetotransport in thin epitaxial  $\text{Bi}_2\text{Se}_3$  films. *JETP Lett.* **104**, 629 (2016).
37. A. G. Stepanov, J. Hebling, and J. Kuhl. Efficient generation of subpicosecond terahertz radiation by phase-matched optical rectification using ultrashort laser pulses with tilted pulse fronts. *Appl. Phys. Lett.* **83**, 3000 (2003).
38. W. Richter, H. Kohler, and C. R. Becker. A Raman and far-infrared investigation of phonons in the rhombohedral  $\text{V}_2\text{-VI}_3$  compounds. *Phys. Status Solidi B* **84**, 619 (1977).
39. A. D. LaForge, A. Frenzel, B. C. Pursley, T. Lin, X. Liu, J. Shi, and D. N. Basov. Optical characterization of  $\text{Bi}_2\text{Se}_3$  in a magnetic field: infrared evidence for magnetoelectric coupling in a topological insulator material. *Phys. Rev. B* **81**, 125120 (2010).
40. Y. Tian, S. Jia, R. J. Cava, R. Zhong, J. Schneeloch, G. Gu, and K. S. Burch. Understanding the evolution of anomalous anharmonicity in  $\text{Bi}_2\text{Te}_{3-x}\text{Se}_x$ . *Phys. Rev. B* **95**, 094104 (2017).
41. L.-D. Zhao, S.-H. Lo, Y. Zhang, H. Sun, G. Tan, C. Uher, C. Wolverton, V. P. Dravid, and M. G. Kanatzidis. Ultralow thermal conductivity and high thermoelectric figure of merit in SnSe crystals. *Nature* **508**, 373 (2014).
42. O. Delaire, J. Ma, K. Marty, A. F. May, M. A. McGuire, M.-H. Du, D. J. Singh, A. Podlesnyak, G. Ehlers, M. Lumsden, B. C. Sales. Giant anharmonic phonon scattering in PbTe. *Nat. Mater.* **10**, 614 (2011).
43. C. W. Li, J. Hong, A. F. May, D. Bansal, S. Chi, T. Hong, G. Ehlers, and O. Delaire. Orbital driven giant phonon anharmonicity in SnSe. *Nat. Phys.* **11**, 1063–1069 (2015).
44. J. A. Johnson, P. D. Salmans, and N. R. Ellsworth. High-Field THz Lattice Control Via Anharmonic Vibrational Coupling. International Conference on Ultrafast Phenomena, OSA Technical Digest (online) (Optical Society of America, 2016), paper UW4A.11.
45. K. N. Boldyrev, T. N. Stanislavchuk, A. A. Sirenko, L. N. Bezmaternykh, and M. N. Popova. Coupling between phonon and crystal-field excitations in multiferroic  $\text{PrFe}_3(\text{BO}_3)_4$ . *Phys. Rev. B* **90**, 121101 (2014).

46. H.-H. Kung, M. Salehi, I. Boulares, A. F. Kemper, N. Koirala, M. Brahlek, P. Lošťák, C. Uher, R. Merlin, X. Wang, S.-W. Cheong, S. Oh, and G. Blumberg. Surface vibrational modes of the topological insulator  $\text{Bi}_2\text{Se}_3$  observed by Raman spectroscopy. *Phys. Rev. B* **95**, 245406 (2017).
47. A. S. Andrushchak, O. V. Yurkevych, O. A. Buryy, V. S. Andrushchak, R. S. Kolodiy, I. M. Solskii, D. Calus, A. Rusek. Spatial anisotropy of the linear electro-optic effect in lithium niobate crystals: Analytical calculations and their experimental verification. *Opt. Mat.* **45**, 42–46 (2015).
48. W. Cheng, S.-F. Ren. Phonons of single quintuple  $\text{Bi}_2\text{Te}_3$  and  $\text{Bi}_2\text{Se}_3$  films and bulk materials. *Phys. Rev. B* **83**, 094301 (2011).